instruments

MDPI

Article

Fabrication and First Full Characterisation of Timing Properties of 3D Diamond Detectors

Lucio Anderlini [1], Marco Bellini [2], Chiara Corsi [3], Stefano Lagomarsino [1], Chiara Lucarelli [1,4], Giovanni Passaleva [1,*], Silvio Sciortino [1,2,4] and Michele Veltri [1,5]

[1] Istituto Nazionale di Fisica Nucleare, Sezione di Firenze, 50019 Sesto Fiorentino, Italy; lucio.anderlini@fi.infn.it (L.A.); stefano.lagomarsino@fi.infn.it (S.L.); chiara.lucarelli@fi.infn.it (C.L.); silvio.sciortino@unifi.it (S.S.); michele.veltri@uniurb.it (M.V.)
[2] Istituto Nazionale di Ottica, Consiglio Nazionale delle Ricerche, 50125 Firenze, Italy; marco.bellini@ino.cnr.it
[3] Laboratorio Europeo Spettroscopie Non Lineari, 50019 Sesto Fiorentino, Italy; corsi@lens.unifi.it
[4] Dipartimento di Fisica e Astronomia, Università degli Studi di Firenze, 50019 Sesto Fiorentino, Italy
[5] Dipartimento di Scienze Pure e Applicate, Università degli Studi di Urbino, 61029 Urbino, Italy
* Correspondence: giovanni.passaleva@fi.infn.it

Abstract: Tracking detectors at future high luminosity hadron colliders are expected to be able to stand unprecedented levels of radiation as well as to efficiently reconstruct a huge number of tracks and primary vertices. To face the challenges posed by the radiation damage, new extremely radiation hard materials and sensor designs will be needed, while the track and vertex reconstruction problem can be significantly mitigated by the introduction of detectors with excellent timing capabilities. Indeed, the time coordinate provides extremely powerful information to disentangle overlapping tracks and hits in the harsh hadronic collision environment. Diamond 3D pixel sensors optimised for timing applications provide an appealing solution to the above problems as the 3D geometry enhances the already outstanding radiation hardness and allows to exploit the excellent timing properties of diamond. We report here the first full timing characterisation of 3D diamond sensors fabricated by electrode laser graphitisation in Florence. Results from a 270 MeV pion beam test of a first prototype and from tests with a β source on a recently fabricated 55×55 μm^2 pitch sensor are discussed. First results on sensor simulation are also presented.

Keywords: detector R&D; timing detectors; diamond; modelling and simulation; laser

Citation: Anderlini, L.; Bellini, M.; Corsi, C.; Lagomarsino, S.; Lucarelli, C.; Passaleva, G.; Sciortino, S.; Veltri, M. Fabrication and First Full Characterisation of Timing Properties of 3D Diamond Detectors. *Instruments* **2021**, *5*, 39. https://doi.org/10.3390/instruments5040039

Academic Editors: Matteo Centis-Vignali, Eraldo Oliveri and Christopher Betancourt

Received: 12 November 2021
Accepted: 13 December 2021
Published: 19 December 2021

1. Introduction

One of the major problems to overcome in the design of tracking detectors at future high luminosity hadron colliders is represented by the unprecedented flux of ionising radiation through the sensors. The expected level of radiation ($\mathcal{O}(10^{16}$–$10^{17})\mathrm{N_{eq}/cm^2}$ [1]) induces severe damage on the sensors over their lifetime and significantly complicates the track and vertex reconstruction problem which may become almost intractable. The invention of 3D solid state detectors [2], with column-like charge-collecting electrodes built in the sensor bulk, provided a very promising solution to these challenges. Firstly, compared to the classical planar geometry, the 3D configuration reduces by about an order of magnitude the charge carrier path towards the electrodes thus reducing the effect of lattice defects induced by radiation. Secondly, the charge collection time is also dramatically reduced down to about 100 ps allowing the realisation of tracking devices with time resolution at the level of 10 ps [3]. The introduction of a precise time information in track hits significantly simplifies the track reconstruction problem, drastically reducing the number of hits that can be associated to a candidate particle trajectory [4].

Diamond has been studied for decades as an ideal semiconductor to obtain extremely radiation hard particle detectors. In more recent years, micro-fabrication of electrodes by laser graphitisation of the crystal bulk [5] enabled the construction of 3D diamond

detectors [6–8] that showed excellent detection properties [9] as well as very promising results on radiation hardness [10]. Only very recently, however, 3D diamond detectors were considered and systematically studied for timing applications, within the TimeSPOT initiative, an R&D project on 3D solid state detectors for timing applications funded by Italian National Institute for Nuclear Physics (INFN) [11]. Charge carriers have much higher mobility and saturation speed in diamond than in silicon, making this material very appealing for timing applications [12]. The 3D geometry, as pointed out before, allows to reach excellent time resolutions making 3D diamond detectors ideal candidates for tracking systems at future accelerators. In this paper, we report on the first full timing characterisation of 3D diamond sensors fabricated by electrode laser graphitisation at the INO-CNR laboratory in Florence. A short summary of the fabrication procedure is given in Section 2; results from a pion beam test and tests with a ^{90}Sr β source of a first prototype are discussed in Sections 3.1 and 3.2; results from a β source test of a recently fabricated $55 \times 55\,\mu m^2$ pitch test sensor are reported in Section 3.3; finally, preliminary simulation studies on our sensors are discussed in Section 4.

2. Sensor Fabrication

The 3D diamond sensors studied in this work were built by fabricating conductive electrodes (or *columns*) in the bulk of 500 µm single crystal Chemical Vapour Deposition (scCVD) [13,14] diamonds produced by Element Six. The electrodes were obtained by laser graphitisation of the diamond with an 800 nm Ti:Sapphire laser with 50 fs pulses focused inside the crystal bulk. Diamond is transparent to 800 nm light, but a sufficiently high light density can result in multiple-photon interactions causing energy absorption through large-bandgap transitions which induce a phase transition from crystalline to mixed carbon phase including graphite. Sufficiently short pulses prevent annealing of graphite into amorphous carbon which is not conductive. To ensure an optimal laser beam focusing, spherical aberrations due to the high diamond refractive index were corrected with a Spatial Light Modulator (SLM) [8,15]. For timing applications, special care has to be paid to the electrode fabrication, since graphitisation is a complex and difficult to control process. According to references [16,17], the generated graphite is concentrated in thin domains embedded in the crystal lattice. Due to this underlying structure, the resistivity of the graphitised electrodes can be rather large which can result in resistances of the order of 10^5–$10^6\,\Omega$ for 500 µm-long electrodes. The high resistivity of electrodes immediately deteriorates the timing properties of the sensors because output signals are attenuated and slowed down. Given a certain electrode resistivity, the resistance could be in principle reduced by increasing the electrode cross-sectional area. However, graphite is significantly less dense than diamond and the graphitisation process generates enormous mechanical stresses within the diamond lattice which may locally crack the crystal. This limits the maximum electrode diameter especially when a fine pitch is required. Other fabrication parameters, like e.g., the pulse energy, duration and frequency, could be tuned to increase the amount of graphite in the electrodes, thus reducing their resistivity.

The column fabrication was made as automatised as possible in order to produce uniform electrodes. Laser parameters and sample movements were controlled through a `python`-based software distributed over a network of processors. Laser parameters were continuously monitored and fed back to the optical system in order to correct for possible drifts from the working point. A run control and a monitoring system have been developed to help the operator to follow the whole fabrication process.

2.1. Fabrication of First Prototype Sensor

A first prototype sensor with 30×30, $55 \times 55\,\mu m^2$ pitch graphite electrodes was built in 2019 on $4.5 \times 4.5\,mm^2$, 500 µm-thick detector grade scCVD by Element Six [11]. The electrodes were fabricated with a prototype optical setup without SLM for spherical aberration correction. We therefore obtained graphitic columns with high resistance of about 100 kΩ–1 MΩ. We grouped several electrodes in larger pads connecting them with

surface graphite traces in various combinations (single strips of variable length, more strips in parallel) that were wire-bonded to seven readout channels. A picture of the first prototype sensor is shown in left panel of Figure 1.

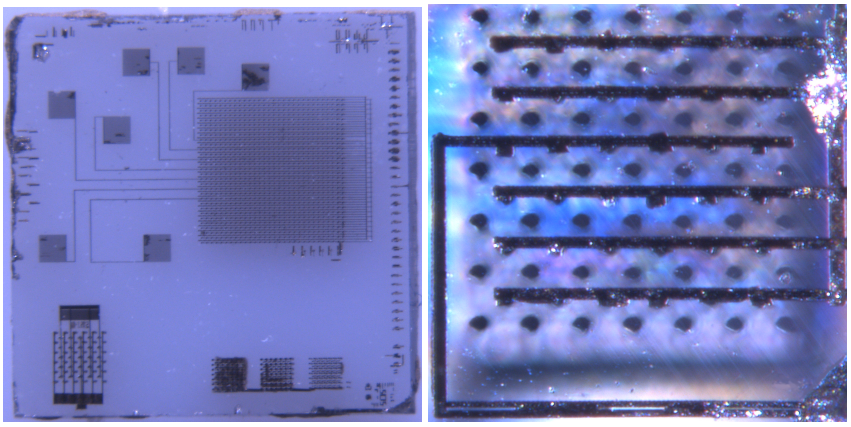

Figure 1. Left: first prototype sensor; the large top-right structure is the 30 × 30 pixel sensor; the square wire bonding pads are also visible on the upper-left quadrant of the sensor. Several test structures are visible at the bottom and around the border of the crystal. **Right**: top view of the new prototype sensor. Black dots are the bias electrodes coming from the crystal back, seen in transparency; black lines are the surface graphitisation contacts to connect the readout electrodes in strips as described in the text.

2.2. Fabrication of New Sensors

A major milestone of TimeSPOT is to test silicon and diamond devices with a novel 28 nm ASIC. The ASIC has 32 × 32 channels with an area of 55 × 55 μm^2 to match the pitch of the TimeSPOT sensors. Each channel features a charge-sensitive amplifier, a discriminator with programmable threshold, and a fully digital time-to-digital converter. More details can be found in Ref. [18]. The chip will be bump-bonded to silicon and diamond 3D pixel detectors by IZM (Fraunhofer-Institut für Zuverlässigkeit und Mikrointegration IZM, Berlin, Germany) and subsequently tested at a particle beam. In preparation for these tests we have fabricated ten new 32 × 32, 55 × 55 μm^2 pitch pixel sensors for bump-bonding to the TimeSPOT ASIC. For the production of this sensor batch, we significantly upgraded our optical system and optimised the fabrication procedure to obtain electrodes with significantly lower resistance. An LCoS-SLM (Hamamatsu X10468-02) for aberration correction as well as a new final focusing objective were introduced in the optical chain. Furthermore, we carried out a systematic optimisation of the fabrication process in order to reduce as much as possible the electrode resistivity without inducing cracks in the diamond lattice, producing and testing more than a thousand test graphitic columns with different processing parameters and different diameters.

Before proceeding with the final production, we built three test sensors with a fabrication procedure optimised for low resistance as resulting from the previous studies. We obtained electrodes with a resistance of ∼30 kΩ which is roughly an order of magnitude smaller than columns of the first prototype. A picture of one of these sensors is shown in the right panel of Figure 1; results from tests of this prototype are discussed in Section 3.3. The pixels are grouped to form two readout channels: a single strip of six pixels (third row from the top in Figure 1, right) and a multiple strip with five connected strips of six pixels each. The single strip is a good proxy of a single pixel while multiple strips simulate clustering of more pixels. This configuration allowed also to study charge sharing effects among pixels.

3. Sensor Test Results

Prototype sensors described in the above sections have been extensively studied with electrons form a ^{90}Sr β source and high energy pions. Preliminary results from these studies are reported in the following sections.

3.1. Test of First Prototype with ^{90}Sr β Source

The first prototype sensor was first tested with electrons form a ^{90}Sr β source in our laboratory. Minimum ionising electrons with energies between ∼1 MeV and ∼2.3 MeV were selected by detecting the Cherenkov light emitted in the 8 mm diameter, 5 mm thick quartz entrance window of a Photonis PP2365Z micro-channel plate photomultuplier (MCP) placed downstream the diamond sensor, which provided also a very precise ($\sigma_t < 20$ ps) time reference. The signals were collected by a readout board by Kansas University [19] and digitised with a high bandwidth (6 GHz) Teledyne Lecroy digital oscilloscope WavePro760Zi-A, and the waveforms saved and analysed offline. The readout board has eight identical channels. Each channel consists of a two stage transimpedance amplifier implemented with Infineon BFP740ESD SiGe wideband transistors in common-emitter configuration. The trigger of the oscilloscope was a qualified trigger armed on the diamond signal and requiring an MCP signal within 10 ns from the diamond signal itself. The threshold on the diamond signal was set to 14 mV with a measured root-mean-square noise of 5.6 mV. The time marker was assigned by a constant-fraction discriminator (CFD) algorithm applied offline to the digitised waveforms. A picture of the experimental setup is shown in Figure 2.

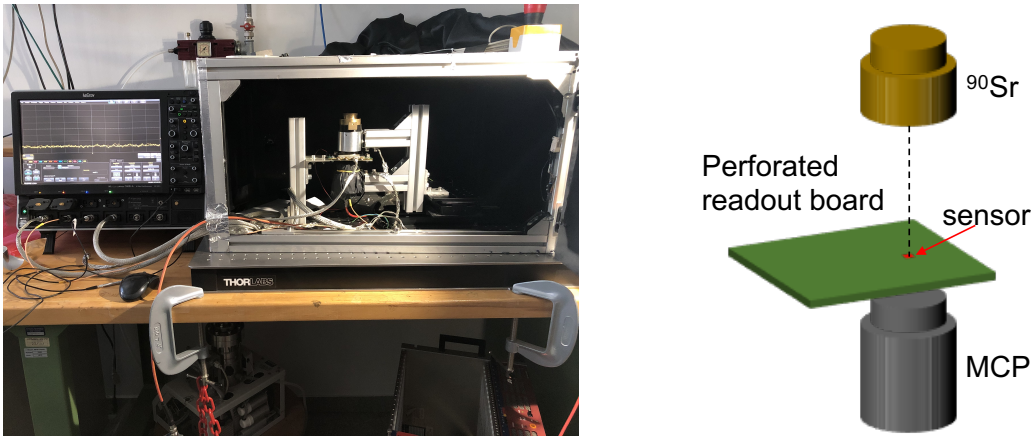

Figure 2. Experimental setup for tests with ^{90}Sr source. On the **left** a picture of the setup; on the **right** a sketch of the source, sensor and MCP arrangement (not to scale).

Due to the very high resistance of the columns, the signals we obtained from the test were significantly attenuated and no Landau peak could be identified due to the modest signal-to-noise (S/N) ratio. The distribution of the time difference between the signal and the reference time given by the MCP ("delay") is reported in the left panel of Figure 3 and shows a prominent tail on the right of the peak. This tail was found to be populated mainly by coincidences with noise or with low amplitude signals, just above threshold, where the CFD algorithm tends to assign delayed time markers because of the signal distortion by the noise The contribution from real MIP signals was isolated on a statistical basis using the ${}_s\mathcal{P}$lot method [20]. From a fit to the delay distribution with a Crystal Ball function (a gaussian core with exponential tails) [21] plus an empirical function to describe the tails due to accidental coincidences [11], a global time resolution $\sigma_{tot} \sim 260$ ps was obtained. The signal amplitude spectrum for MIP signals is also reported in Figure 3; the time resolution as a function of signal amplitude is overlaid showing that the resolution for the larger signals tends asymptotically to $\sigma_{asy} \sim 170$ ps.

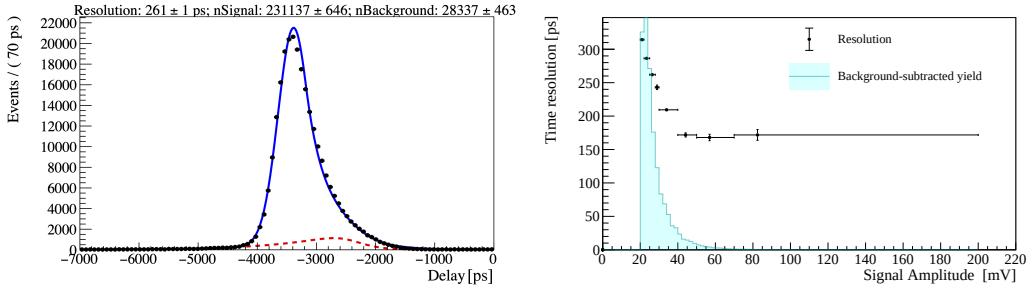

Figure 3. Left: distribution of the time difference between signal and trigger (delay) for electrons from the ^{90}Sr source. The blue continuous curve represents the fit to the distribution with a Crystal Ball function plus an empirical function for the random coincidence background (red dashed curve). The fitted number of true (nSignal) and accidental (nBackground) coincidences is given on top of the plot. **Right**: amplitude spectrum for the signals populating the delay distribution (light blue histogram); the time resolution in bins of signal amplitude is overlaid (black full circles).

3.2. Test of First Prototype with High Energy Pions

The same prototype was also tested in 2019 at the 270 MeV/c πM1 pion beam of Paul Scherrer Institute (PSI) in Villigen, Switzerland. Minimum ionising pions were selected with two Cherenkov counters obtained with quartz radiators read out by large area $(5.3 \times 5.3\,\mathrm{cm}^2)$ Photonis Planacon XP85112 MCPs. Signals were acquired with the same readout chain described above using the same oscilloscope trigger configuration and threshold, with the two MCPs in logical AND. The delay distribution and amplitude spectrum of signals are very similar to those obtained with the β source. Therefore, also for these data the separation of true from accidental coincidences was obtained with the ${}_s\mathcal{P}$lot method, yielding a global time resolution $\sigma_{\mathrm{tot}} \sim 240$ ps. The delay distribution is shown in Figure 4. The larger accidental coincidence background with respect to measurements made with β electrons is due to the much larger area of the MCPs used for trigger at PSI. The time resolution as a function of signal amplitude for pion data is also shown, overlaid to the amplitude spectrum. The amplitude dependent time resolution for the electron sample is also shown on the same plot for comparison: the two distributions are in good agreement.

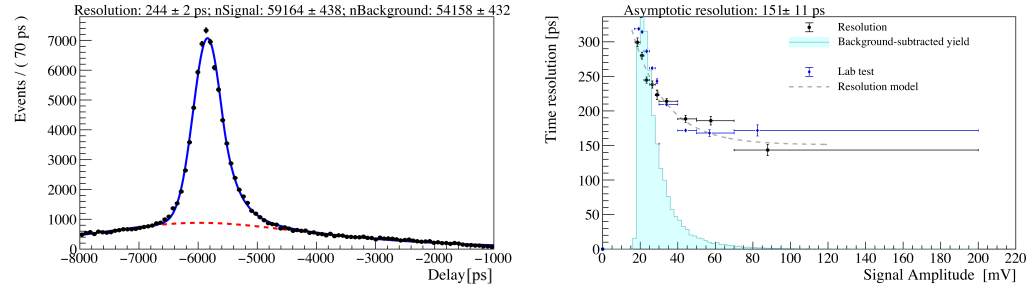

Figure 4. Left: distribution of the time difference between signal and trigger (delay) for 270 MeV/c pions. The blue continuous curve represents the fit to the distribution with a Crystal Ball function plus an empirical function for the random coincidence background (red dashed curve). The fitted number of true (nSignal) and accidental (nBackground) coincidences is given on top of the plot. **Right**: amplitude spectrum for the signals populating the delay distribution (light blue histogram); the time resolution in bins of signal amplitude for pions (black full circles) and electrons (blue full diamonds) is overlaid; a fit of the pion resolution with a simplified resolution model (see text) is also shown (grey dashed curve).

The time resolution as a function of the amplitude A follows with reasonable agreement the simple model

$$\sigma_t = \sqrt{\sigma_{asy}^2 + (\sigma_{noise} \cdot \bar{t}_{rise})^2 / A^2}, \quad (1)$$

where σ_{noise} is the electronics noise, $\bar{t}_{rise}$ is the average signal rise time, and σ_{asy} is the resolution that could be obtained in the absence of any noise. This simplified model of time resolution takes into account only the main contribution given by the noise to signal slope ratio (see for example ref. [4]), which dominates given the observed small signal-to-noise ratio. A fit to the data with the above model is shown by the grey dashed curve in Figure 4 (right), which gives an asymptotic resolution $\sigma_{asy} \sim 150$ ps.

3.3. *Preliminary Results on New Sensors with* ^{90}Sr *Source*

The new prototype sensor was extensively tested using the ^{90}Sr β source with a readout system identical to that described in Section 3.1. Due to the divergence of the electrons from the source, the large multiple scattering affecting electrons and the 1:10 pixel aspect ratio, significant amount of charge was released by electrons outside a single pixel. The substantial charge sharing effect could be studied and corrected for by summing coincidence signals of the single and multiple pixel strips described above. The amplitude spectrum of signals from the single strip is shown in Figure 5 (left panel, blue full markers). No clear peak is visible in the spectrum; however, by summing the charge released in the neighbouring cells, as measured in coincidence by the multiple strip channel, an evident Landau peak emerges that can be well discriminated from the noise (left panel, red full markers). This is also visible in the spectrum of multiple strip channel, although with a slightly worse S/N ratio (Figure 5, right). The larger S/N ratio obtained with respect to the first prototype is a first clear effect of the lower electrode resistance.

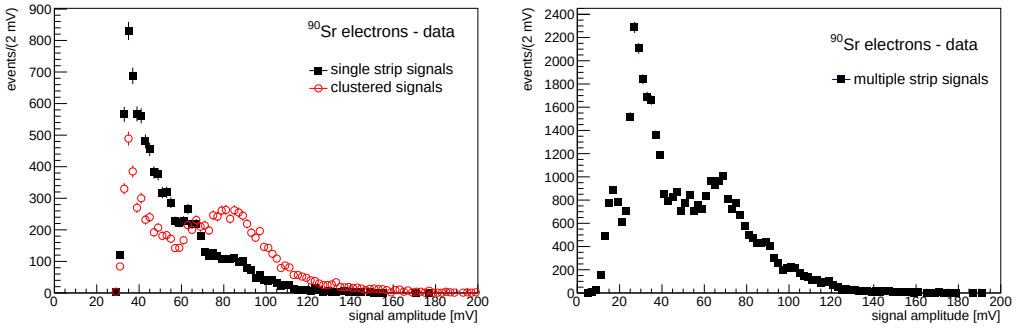

Figure 5. Left: signal amplitude spectrum of single-strip channel (black full squares); summing the amplitude of signals of neighbouring pixels, the red open circle histogram is obtained. **Right**: signal amplitude spectrum of multiple-strip channel.

Results from a data set obtained with a threshold of 40 mV are shown in Figure 6. The delay distribution is now background free but shows still a slightly asymmetric tail on the right of the delay distribution. This tail is probably due to the effect of the surface graphitic tracks running just outside the sensor fiducial area (used to connect the pixels to the bonding pads; see Figure 1, right), which produce fringe electric field where the charge collection is presumably slower than in the pixels. This effect can not be easily disentangled with the β source and will be studied in detail in an upcoming beam test, where precise fiducial regions inside the sensor will be selected using a collimating 55×55 μm^2 TimeSPOT single pixel silicon sensor. A fit with a Crystal Ball function yields a global time resolution $\sigma_{tot} = 120$ ps a factor of two better than that obtained with the first prototype. The time resolution as a function of the signal amplitude follows fairly well the simple model of Equation (1) and gives a time resolution for large signals $\sigma_{asy} \sim 75$ ps.

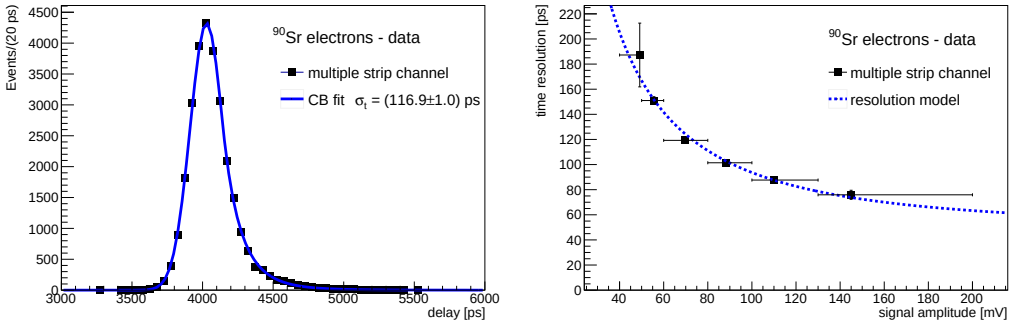

Figure 6. New prototype results: distribution of time difference between diamond and MCP signals, for ^{90}Sr electron signals larger than 40 mV (**left**); the time resolution is obtained from a fit (superimposed blue full line) with a crystal ball function. Time resolution in bins of signal amplitude (**right**); the blue dashed line is the fitted simplified resolution model.

4. Sensor Simulation Results

In order to facilitate the interpretation of experimental results and study possible optimisations, we started a simulation campaign to study the main features of 3D diamond sensors from timing point of view. Material models of diamond are not normally included by default in most of the professional solid state device simulation tools such as for example Synopsys© Sentaurus `TCAD` and must therefore be explicitly implemented [22]. Detailed `TCAD` simulations of diamond 3D detectors have been performed by several authors (e.g., [23]); however `TCAD` simulation is rather computing intensive, thus not particularly suitable for simulation of large statistics samples. In this study we therefore chose to simulate the electric fields and charge transport with the ROOT-based [24] simulator `KDetSim` [25].

4.1. Simulation Flow

The simulation flow starts with a detailed `Geant4` [26,27] simulation of the ^{90}Sr available at our laboratory, of a 270 MeV pion beam, and of the experimental test setup. The diamond sensor is schematised as a 3×3 pixel matrix uniformly illuminated by incident particles, but only the particle charge deposits in the central pixel are considered for further processing. The charge carriers are drifted in the electric field through the `KDetSim` package; the simulated electric field and potential are shown in Figure 7. Given their large per-unit-length resitance and their aspect ratio, the resistive electrodes are modelled as lossy transmission lines (an alternative model with a "ladder-like" discrete set of series resistors and parallel capacitors gave largely compatible results). The signal currents obtained from `KDetSim` are thus convoluted with the electrode and electronics impulse response functions, following the recipe described in [28].

For this study, no noise simulation has been attempted and we used real data noise waveforms superimposed to simulated signals. The simulated waveforms are finally processed with the same algorithms used for data. The distribution of the total charge released by pions and electrons, as obtained from `Geant4` simulation is shown in the left panel of Figure 8. A prominent Landau peak is well visible in the pion spectrum while the electron spectrum is broader, due to the underlying β energy spectrum. The distribution of the charge released by pions and electrons in the central pixel, is shown instead on the right panel of Figure 8. It can be seen that, as expected, in the case of electrons a considerable amount of charge leaks outside the pixel volume. As a result, signals from β electrons are generally smaller and only a broad peaking structure is expected. Pions instead generate larger signals with a clear peak with a characteristic tail of small signals on the left of the most probable value, due mostly to δ-rays or tracks leaving the pixel volume.

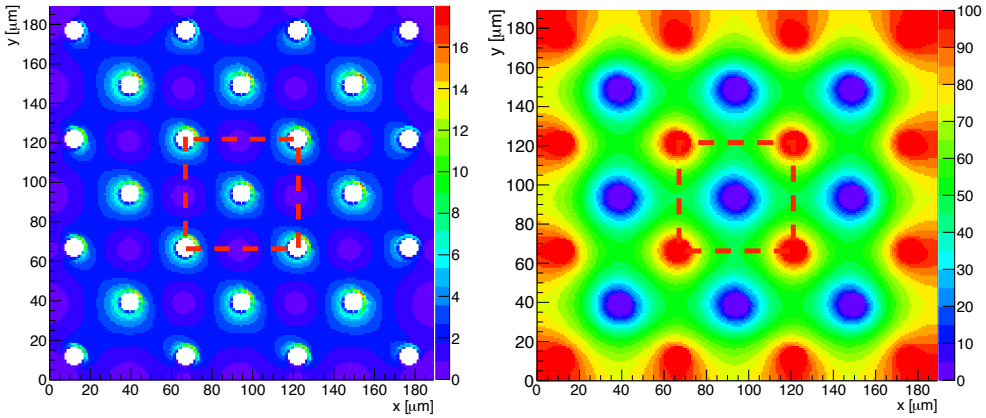

Figure 7. Electric field (in V/μm, **left** panel) and potential (in V, **right** panel) for a 3 × 3 pixel matrix calculated with `KDetSim`. The red-dashed square indicates the active area of the central pixel.

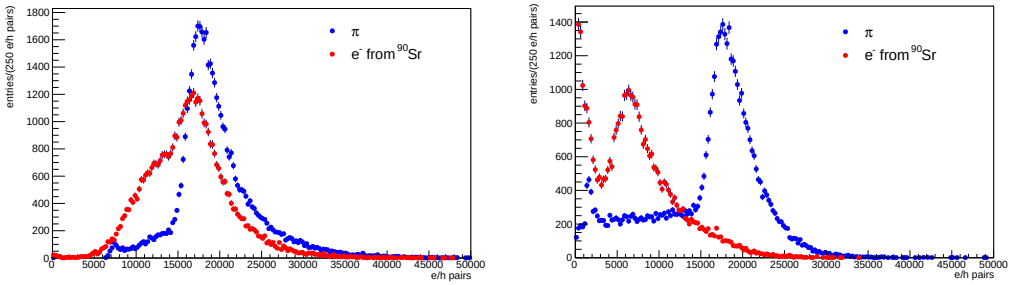

Figure 8. Charge released in a 3 × 3 pixel matrix and in a single 55 × 55 μm pixel (left) by ^{90}Sr electrons and 270 MeV pions, expressed in number of electron-hole pairs, obtained from the `Geant4` simulation.

4.2. Simulation Results

The simulation flow has been validated with data obtained from the single-strip channel of the 55 × 55 μm^2 test sensor irradiated with the ^{90}Sr β source. The data were acquired with a trigger threshold of 30 mV and their signal spectrum is shown in Figure 5 (left panel, black square markers). As expected, this sample has a significantly lower S/N ratio with respect to data collected with the multiple-strip channel, due to the large multiple scattering of electrons. However, as discussed in Section 2.2, the single strip is a better proxy of a single pixel, and is therefore more directly comparable with the simulation. In the simulation, the electrode resistance was assumed to be 30 kΩ.

The comparison between data and simulation was performed on distributions of delay between the MCP trigger and signal time markers, of signal amplitude, and of rise time. All the distributions were normalised to unit area. As shown in Figure 9, reasonably good agreement between data and simulation is observed in all considered distributions, confirming an overall good description of the signal generation and acquisition chain.

A comparison of the time resolution obtained with the same data and simulated signals is reported in Figures 10 and 11, showing an overall good agreement between data and simulation. As can be seen from Figure 9 top panel and Figure 10 left panel, the asymmetric tail on the right of the delay distribution is more prominent than in the case of data from the multiple-strip channel, confirming that it is mainly populated by accidental coincidences with noise. This effect is reproduced by the simulation as can be seen from Figure 9 and comparing left and right panels of Figure 10, although with a residual disagreement with data. The tail on the right is indeed slightly larger in data than in the simulation. We think that this residual disagreement is due to the effect of the graphitic structures discussed in Section 3.3, which are not taken into account in the simulation. Nevertheless, further investigations will be needed to clarify this discrepancy.

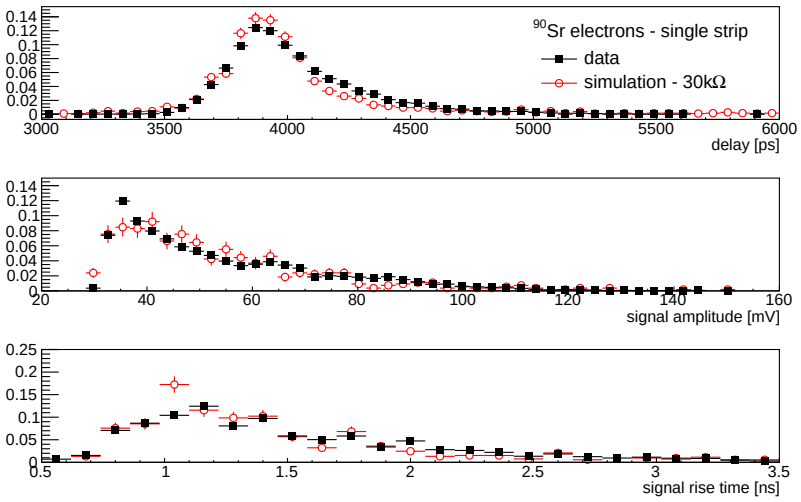

Figure 9. Data distributions of delay (**top**), amplitude (**middle**) and rise time (**bottom**), for ^{90}Sr electrons compared with simulation.

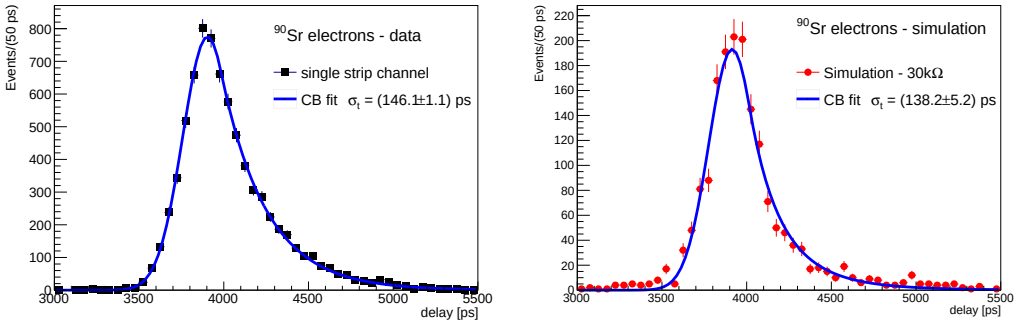

Figure 10. Time resolution for ^{90}Sr electrons from data (**left**) and simulated signals (**right**).

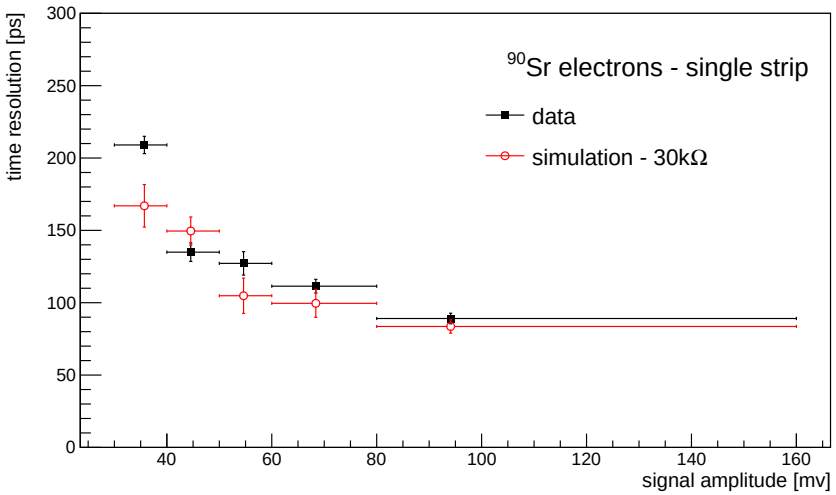

Figure 11. Time resolution as a function of signal amplitude for data (black squares) and simulated (red circles) ^{90}Sr electrons.

The simulation results will be further validated shortly in a beam test with high energy hadrons. Further tests will be carried out when the sensors will be bump-bonded on the TimeSPOT ASIC.

After validation, the simulation was used to study the time resolution as a function of the electrode resistance which is, at the current stage of the development, the main driving parameter for timing performance. The same pixel matrix described in Section 4.1

was simulated with electrodes of different resistance ranging from 1 kΩ to 40 kΩ, using both β electrons and minimum ionising pions. The results are shown in Figure 12. The simulation confirms the expectation that the time resolution improves substantially when the resistance of the electrodes diminishes, thanks to an increasing S/N ratio.

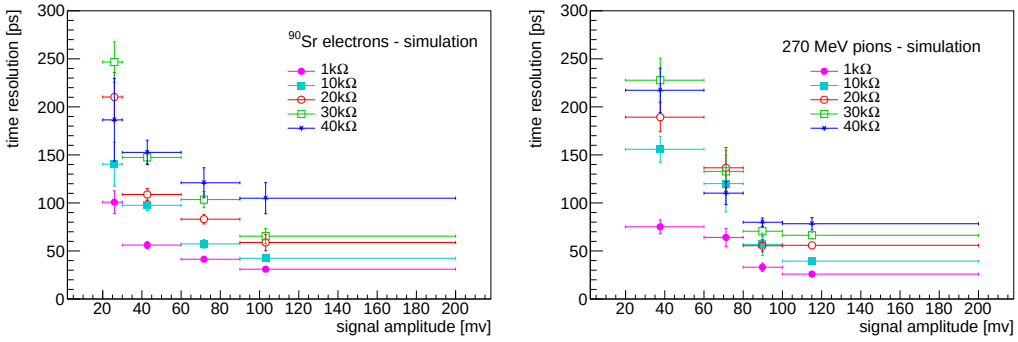

Figure 12. Time resolution as a function of signal amplitude for simulated ^{90}Sr electrons (**left**) and 270 MeV pions (**right**), for different values of the electrode resistance.

5. Conclusions

An intense R&D program on 3D diamond detectors for timing applications has been going on in Florence in the framework of the TimeSPOT initiative. A first beam test held at PSI successfully demonstrated the potential of these devices for 4D tracking. Preliminary laboratory results with recently fabricated 55×55 μm^2 pitch 3D sensors show very encouraging results hinting at possible time resolutions in the range of 70–80 ps or better. At the current stage, the main limiting parameter is the resistance of the electrodes that slows down the signals and reduces their amplitude when they are fed into fast electronics. We are therefore investing significant effort in optimising the sensor fabrication procedure in order to minimise the electrode resistance.

Furthermore, in order for this technology to become viable for large scale tracking systems, additional developments will need to be carried out in order to make the fabrication procedure scalable to larger areas and larger number of sensors.

These tests were a first validation of the fabrication procedure used to construct ten 32×32, 55×55 μm^2 pitch pixel sensors which will be bump-bonded on 28 nm TimeSPOT ASIC at IZM and will be tested at a high energy particle beam test.

Author Contributions: Conceptualization, G.P., L.A., S.L. and S.S.; methodology, C.L., G.P., L.A. and M.V.; resources, M.B. and C.C.; formal analysis, C.L., G.P., L.A. and M.V.; investigation, C.C., C.L., G.P., L.A., M.B., M.V., S.L. and S.S.; software, C.L., G.P., L.A. and M.V.; writing—original draft preparation, G.P. All authors have read and agreed to the published version of the manuscript.

Funding: This research was funded by INFN as part of the TimeSPOT initiative.

Institutional Review Board Statement: Not applicable.

Informed Consent Statement: Not applicable.

Data Availability Statement: Data and software used in this research are freely available from the authors on request.

Acknowledgments: The authors would like to acknowledge N. Minafra from the University of Kansas for providing the readout boards used in this research and for fruitful discussions and invaluable support in the interpretation of data. Very useful discussions with W. Riegler (CERN) on detector simulation are also gratefully acknowledged. The authors finally gratefully acknowledge the highly qualified technical support by M. Brianzi (INFN) and S. Nocentini (CNR-INO).

Conflicts of Interest: The authors declare no conflict of interest. The funders had no role in the design of the study; in the collection, analyses, or interpretation of data; in the writing of the manuscript, or in the decision to publish the results.

References

1. Abada, A.; Abbrescia, M.; AbdusSalam, S.S.; Abdyukhanov, I.; Abelleira Fernandez, J.; Abramov, A.; Aburaia, M.; Acar, A.O.; Adzic, P.R.; Agrawal, P.; et al. FCC-hh: The Hadron Collider. *Eur. Phys. J. Spec. Top.* **2019**, *228*, 755–1107. [CrossRef]
2. Parker, S.; Kenney, C.; Segal, J. 3D—A proposed new architecture for solid-state radiation detectors. *Nucl. Instrum. Methods Phys. Res. Sect. A Accel. Spectrometers Detect. Assoc. Equip.* **1997**, *395*, 328–343. doi: 10.1016/S0168-9002(97)00694-3. [CrossRef]
3. Anderlini, L.; Aresti, M.; Bizzeti, A.; Boscardin, M.; Cardini, A.; Dalla Betta, G.F.; Ferrero, M.; Forcolin, G.; Garau, M.; Lai, A.; et al. Intrinsic time resolution of 3D-trench silicon pixels for charged particle detection. *JINST* **2020**, *15*, P09029. [CrossRef]
4. Sadrozinski, H.F.W.; Seiden, A.; Cartiglia, N. 4D tracking with ultra-fast silicon detectors. *Rep. Prog. Phys.* **2017**, *81*, 026101. [CrossRef] [PubMed]
5. Kononenko, T.; Komlenok, M.; Pashinin, V.; Pimenov, S.; Konov, V.; Neff, M.; Romano, V.; Läthy, W. Femtosecond laser microstructuring in the bulk of diamond. *Diam. Relat. Mater.* **2009**, *18*, 196–199. [CrossRef]
6. Oh, A.; Caylar, B.; Pomorski, M.; Wengler, T. A novel detector with graphitic electrodes in CVD diamond. *Diam. Relat. Mater.* **2013**, *38*, 9–13. [CrossRef]
7. Caylar, B.; Pomorski, M.; Bergonzo, P. Laser-processed three dimensional graphitic electrodes for diamond radiation detectors. *Appl. Phys. Lett.* **2013**, *103*, 043504. [CrossRef]
8. Sun, B.; Salter, P.S.; Booth, M.J. High conductivity micro-wires in diamond following arbitrary paths. *Appl. Phys. Lett.* **2014**, *105*, 231105. [CrossRef]
9. Lagomarsino, S.; Bellini, M.; Corsi, C.; Gorelli, F.; Parrini, G.; Santoro, M.; Sciortino, S. Three-dimensional diamond detectors: Charge collection efficiency of graphitic electrodes. *Appl. Phys. Lett.* **2013**, *103*, 233507. [CrossRef]
10. Lagomarsino, S.; Bellini, M.; Corsi, C.; Cindro, V.; Kanxheri, K.; Morozzi, A.; Passeri, D.; Servoli, L.; Schmidt, C.J.; Sciortino, S. Radiation hardness of three-dimensional polycrystalline diamond detectors. *Appl. Phys. Lett.* **2015**, *106*, 193509. [CrossRef]
11. Anderlini, L.; Bellini, M.; Bizzeti, A.; Cardini, A.; Ciaranfi, R.; Corsi, C.; Garau, M.; Lai, A.; Lagomarsino, S.; Lampis, A.; et al. Fabrication and Characterisation of 3D Diamond Pixel Detectors With Timing Capabilities. *Front. Phys.* **2020**, *8*, 589844. [CrossRef]
12. Bossini, E.; Minafra, N. Diamond Detectors for Timing Measurements in High Energy Physics. *Front. Phys.* **2020**, *8*, 248. [CrossRef]
13. Gracio, J.J.; Fan, Q.H.; Madaleno, J.C. Diamond growth by chemical vapour deposition. *J. Phys. D Appl. Phys.* **2010**, *43*, 374017. [CrossRef]
14. Schwander, M.; Partes, K. A review of diamond synthesis by CVD processes. *Diam. Relat. Mater.* **2011**, *20*, 1287–1301. [CrossRef]
15. Salter, P.S.; Baum, M.; Alexeev, I.; Schmidt, M.; Booth, M.J. Exploring the depth range for three-dimensional laser machining with aberration correction. *Opt. Express* **2014**, *22*, 17644–17656. [CrossRef] [PubMed]
16. Salter, P.S.; Booth, M.J.; Courvoisier, A.; Moran, D.A.J.; MacLaren, D.A. High resolution structural characterisation of laser-induced defect clusters inside diamond. *Appl. Phys. Lett.* **2017**, *111*, 081103. [CrossRef]
17. Ashikkalieva, K.; Kononenko, T.; Obraztsova, E.; Zavedeev, E.; Khomich, A.; Ashkinazi, E.; Konov, V. Direct observation of graphenic nanostructures inside femtosecond-laser modified diamond. *Carbon* **2016**, *102*, 383–389. [CrossRef]
18. Piccolo, L.; Rivetti, A.; Cadeddu, S.; Casu, L.; Lai, A.; Barbaro, M.; Napoli, C.; Sonedda, S.; Frontini, L.; Liberali, V.; et al. The first ASIC prototype of a 28 nm time-space front-end electronics for real-time tracking. *PoS* **2020**, *TWEPP2019*, 022. [CrossRef]
19. Minafra, N.; Al Ghoul, H.; Arcidiacono, R.; Cartiglia, N.; Forthomme, L.; Mulargia, R.; Obertino, M.; Royon, C. Test of Ultra Fast Silicon Detectors for picosecond time measurements with a new multipurpose read-out board. *Nucl. Instrum. Methods Phys. Res. Sect. A Accel. Spectrometers Detect. Assoc. Equip.* **2017**, *867*, 88–92. [CrossRef]
20. Pivk, M.; Le Diberder, F. sPlot: A statistical tool to unfold data distributions. *Nucl. Instrum. Methods Phys. Res. Sect. A Accel. Spectrometers Detect. Assoc. Equip.* **2005**, *555*, 356–369. [CrossRef]
21. Skwarnicki, T. A Study of the Radiative Cascade Transitions between the Upsilon-Prime and Upsilon Resonances. Ph.D. Thesis, Institute of Nuclear Physics, Krakow, Poland, 1986.
22. Morozzi, A.; Passeri, D.; Kanxheri, K.; Servoli, L.; Lagomarsino, S.; Sciortino, S. Polycrystalline CVD diamond device level modeling for particle detection applications. *J. Instrum.* **2016**, *11*, C12043. [CrossRef]
23. Morozzi, A.; Sciortino, S.; Anderlini, L.; Servoli, L.; Kanxheri, K.; Lagomarsino, S.; Passeri, D. 3D Diamond Tracking Detectors: Numerical analysis for Timing applications with TCAD tools. *J. Instrum.* **2020**, *15*, C01048. [CrossRef]
24. Brun, R.; Rademakers, F. ROOT: An object oriented data analysis framework. *Nucl. Instrum. Meth. A* **1997**, *389*, 81–86. [CrossRef]
25. Kramberger, G. KDetSim—A Simple Way to Simulate Detectors. 2016. Available online: https://github.com/IJSF9Software/KDetSim (accessed on 12 December 2021).
26. Agostinelli, S.; Allison, J.; Amako, K.A.; Apostolakis, J.; Araujo, H.; Arce, P.; Asai, M.; Axen, D.; Banerjee, S.; Barr, G.J.N.I.; et al. Geant4: A simulation toolkit. *Nucl. Instrum. Meth.* **2003**, *A506*, 250. [CrossRef]
27. Allison, J.; Amako, K.; Apostolakis, J.; Araujo, H.; Dubois, P.; Asai, M.; Barrand, G.; Capra, R.; Chauvie, S.; Chytracek, R.; et al. Geant4 developments and applications. *IEEE Trans. Nucl. Sci.* **2006**, *53*, 270. [CrossRef]
28. Riegler, W.; Windischhofer, P. Signals induced on electrodes by moving charges, a general theorem for Maxwell's equations based on Lorentz-reciprocity. *Nucl. Instr. Meth. A* **2020**, *980*, 164471. [CrossRef]